OPEN ACCESS

Fast Redox Kinetics in $SrCo_{1-x}Sb_xO_{3-\delta}$ Perovskites for Thermochemical Energy Storage

To cite this article: George E. Wilson *et al* 2022 *J. Electrochem. Soc.* **169** 044509

Journal of The Electrochemical Society, 2022 **169** 044509

Fast Redox Kinetics in $SrCo_{1-x}Sb_xO_{3-\delta}$ Perovskites for Thermochemical Energy Storage

George E. Wilson,[1] Ieuan D. Seymour,[1] Andrea Cavallaro,[1] Stephen J. Skinner,[1,*,z] and Ainara Aguadero[1,2]

[1]*Department of Materials, Imperial College London, Exhibition Road, London SW7 2AZ, United Kingdom*
[2]*Instituto de Ciencia de Materiales de Madrid, CSIC, 28049, Cantoblanco, Madrid, Spain*

The use of perovskite materials for thermochemical energy storage and oxygen separation has been gaining momentum in recent years due to their ability to topotactically exchange large volumes of oxygen, and their chemical and structural flexibility. B-site substituted $SrCoO_{3-\delta}$ derivatives have previously been investigated as promising materials for intermediate temperature solid oxide fuel cell cathodes due to the stabilization of a 3 C perovskite structure with high electronic and ionic conductivity that allows large oxygen storage capabilities. Here, antimony-substituted strontium cobalt oxides are investigated and identified as new candidate materials for thermochemical oxygen separation applications. In this work we shed light on the exceptional redox kinetics and cyclability of antimony-substituted variants undergoing oxygen exchange at intermediate temperatures (500 to 800 °C). Through the use of density functional theory and isothermal gas atmosphere switching, we demonstrate how the inductive effect of the more electronegative antimony dopants in the Co position, facilitates the kinetics of metal oxide oxidation, whilst hindering reduction reactions. $SrCo_{0.95}Sb_{0.05}O_{3-\delta}$ was identified to isothermally evolve 3.76 $cm^3\ g^{-1}$ of oxygen at 500 °C and calculated to produce up to 10.44 $cm^3\ g^{-1}$ under temperature-swing reaction configurations aligning with previously reported materials.
 [DOI: 10.1149/1945-7111/ac62c5]

Manuscript submitted December 15, 2021; revised manuscript received March 14, 2022. Published April 8, 2022. *This paper is part of the JES Focus Issue on Focus Issue In Honor of John Goodenough: A Centenarian Milestone.*

Supplementary material for this article is available online

Solar energy can theoretically provide surplus amounts of energy, in excess of current societal demands, and could meet future growth. However, the current commercial photovoltaic technologies utilize only a fraction of the solar spectrum. Concentrated solar power technologies provide an alternative solution that makes use of the whole solar spectrum by using heliostat mirrors to concentrate and heat a central receiver.[1] Within the central receiver, the thermal energy can be stored by sensible heat (in the form of molten salts),[2,3] latent heat—in the form of phase change materials,[4,5] and thermochemical—by thermal reduction of a reactant and subsequent release of molecules.[6] Thermochemical methods lead to the possibility of high energy storage density due to their design simplicity and long-term storage potential, however they are not industrially progressed with many new families of materials still being researched.

In thermochemical technologies, solar energy is stored during an initial reduction step where the materials are thermally reduced and consequently release oxygen molecules from their structure, causing an oxygen deficiency (δ) within the structure (Eq. 1). The extent to which a material can accommodate the oxygen deficiency within the lattice, whilst remaining stable, is known as the oxygen storage capability, and greater values allow for greater energy storage. This value can be increased further by heating under low oxygen partial pressures induced by an inert sweep gas or vacuum.

$$ABO_3 + \Delta H \rightarrow ABO_{3-\delta} + \frac{\delta}{2}O_2 \quad [1]$$

where A and B are both metal cations and ΔH is thermal energy.

The stored energy is subsequently released through an exothermic reaction when the oxygen is reincorporated into the lattice and reoxidizes the metal oxide (Eq. 2). This oxidation step is carried out by cooling the reduced metal oxide to lower temperatures or increasing the oxygen partial pressure. These are known as temperature-swing and pressure-swing operating modes respectively.

$$ABO_{3-\delta} + \frac{\delta}{2}O_2 \rightarrow ABO_3 + \Delta H \quad [2]$$

Hydride,[7] carbonate,[8,9] and hydroxide[10,11] materials have been extensively researched for thermochemical energy storage materials. These materials all require closed gas systems and have associated safety concerns. Oxide materials have the advantage of utilizing oxygen from the atmosphere thus removing the need for gas storage systems. Co_3O_4, which adopts the spinel structure, has exceptionally large energy storage capability (844 kJ kg^{-1}) and long term cyclability.[12–15] Other binary transition metal oxides such as Fe_3O_4[16] and Mn_2O_3[17] have been investigated as lower-cost alternatives however the oxygen migration within these materials is slow, and has motivated the field to move towards topotactic non-stoichiometric oxides, such as perovskites.[6] This class of metal oxides have a wide chemical flexibility that allows tuning and optimization of reaction kinetics, storage capabilities and structural stability.[6,18–22] $CaMnO_3$ and its substituted variants has been well reported for good energy storage densities.[19] This was increased further by the incorporation of low strontium concentrations (<10%) onto the A-site, with reported thermochemical energy storage capacities of up to 555 kJ kg^{-1} at 1000 °C,[23] however this is still much lower than the cobalt oxide system. However, the release and reincorporation of oxygen from metal oxide lattices has been used in other technologies such as chemical looping air separation or oxygen separation.[24–26] The combustion of fuels under rich oxygen conditions produces an easily separated mixture of CO_2 and H_2O. However, current methods for pure oxygen production are energy intensive. The oxygen released from metal oxides is inherently pure and can be easily replenished from air. $SrFeO_{3-\delta}$ is one perovskite that has been heavily studied for this process demonstrating fast redox kinetics.[27] Further efforts aimed to increase the oxygen storage content by including cobalt onto the B-site.[28–30]

A computational study by Ezbiri et al. identified cubic $SrCoO_3$ at the top of a Sabatier plot for thermochemical oxygen separation, which has optimal energetics for both vacancy formation and oxygen incorporation.[31] Although the reduction enthalpies reported were lower than thermochemical energy storage perovskites, the material

*Electrochemical Society Member.
[z]E-mail: s.skinner@imperial.ac.uk

exhibited redox cycling behavior but their work was not expanded to understand the kinetics. Fortunately, there is a large field of literature on strontium cobalt perovskites demonstrating their topotactic redox behavior for applications such as cathode materials in intermediate solid oxide fuel cells[32–34] and bifunctional oxygen electrocatalysts.[35,36]

The cubic structure of undoped $SrCoO_3$ is unstable below 900 °C and upon slow cooling the cubic phase segregates into a rhombohedral 2H-type $Sr_6Co_5O_{15}$ structure and a Co_3O_4 spinel phase.[37] The former rhombohedral polymorph contains a one-dimensional series of 4 face sharing CoO_6 octahedra between every Co oxide triangular prism.[38] A recent study by Pan et al.[36] suggested that the oxygen evolution reaction within strontium cobaltite is mainly limited by the lattice oxygen diffusion. The stabilization of a 3 C perovskite array (cubic perovskite with corner sharing BO_6 octahedra) at room temperature leads to an improvement of the thermal stability, oxygen mobility and total conductivity which can be achieved through the incorporation of larger radii, higher valency cations onto the B-site.[32–34] The substitutional elements lower the Goldschmidt tolerance factor and reduce the cobalt to the more thermodynamically favorable 3+ oxidation state, thus stabilizing a 3 C perovskite arrangement that due to oxygen vacancy ordering is stabilized in the tetragonal *P4/mmm* space group.[39] The corner sharing polyhedral network promotes 3-dimensional oxygen diffusion within the structure. Out of the large number of dopants that have been tested, antimony has shown some of the most interesting features in terms of oxygen storage capacities and electrical properties which make it a great candidate for fast thermochemical storage.[39–41]

In this work, we investigate the effect of *B*-site substituted $SrCo_{1-x}Sb_xO_{3-\delta}$ as new candidate materials for thermochemical energy storage and oxygen separation applications in the 500 to 800 °C temperature range using simultaneous thermal analysis techniques combined with computational density functional theory methods.

Materials and Methods

Synthesis and characterization.—$SrCo_{1-x}Sb_xO_{3-\delta}$ (x = 0.05, 0.10 and 0.20) powders were synthesized using a nitrate-citrate method, as previously reported.[39–41] Stoichiometric ratios of precursor powders $Sr(NO_3)_2$ (>99%, Sigma Aldrich), $Co(NO_3)_2{\cdot}6H_2O$ (Alfa Aesar) and Sb_2O_3 (99%, Alfa Aesar) were weighed and added to a stirring solution of 0.1 M citric acid (aq. 1% (v/v) 68% nitric acid). The solution was heated to a nominal temperature of 60 °C resulting in complete dissolution, followed by heating to 300 °C to promote the sol-gel reaction. The crude gel was decomposed at 600 °C for 12 h before further calcination steps at 900, 1000 and 1100 °C for 12, 24 and 24 h, respectively, with intermediary grinding stages using a pestle and mortar.

The crystal structure of the synthesized powders was characterized using X-ray powder diffraction (XRD). A Panalytical MPD was used with Cu-Kα radiation (λ = 1.542 Å) in a Bragg-Brentano setup. All measurements used the following parameters; $20° < 2\theta < 80°$ and 0.04° step size with 100 seconds per step. A JEOL 6010LA scanning electron microscope (SEM) was used to assess the particle morphology before and after the gas switching experiments.

Thermal analysis.—The thermal behavior and redox cyclability of the powders were investigated using a simultaneous thermal analyzer (STA) (Netzsch 449c F5). This instrument combines thermogravimetric analysis (TGA) in tandem with differential scanning calorimetry (DSC). The oxygen concentration in the exhaust was investigated using an oxygen sensor (Rapidox 2100 Gas Analyzer). Approximately 50 mg of powder was loaded into a platinum crucible. A similar mass of calcined alumina was used as a reference. The TGA chamber was twice evacuated using a scroll pump and backfilled with argon to achieve an environment with 20 ppm oxygen partial pressure. This provided a low partial pressure to both promote thermal reduction of the metal oxide and allow for oxygen production volumes to be recorded. In all thermal analysis experiments, pure and dry gases were used to limit the effect of water-induced surface phase decomposition.[42]

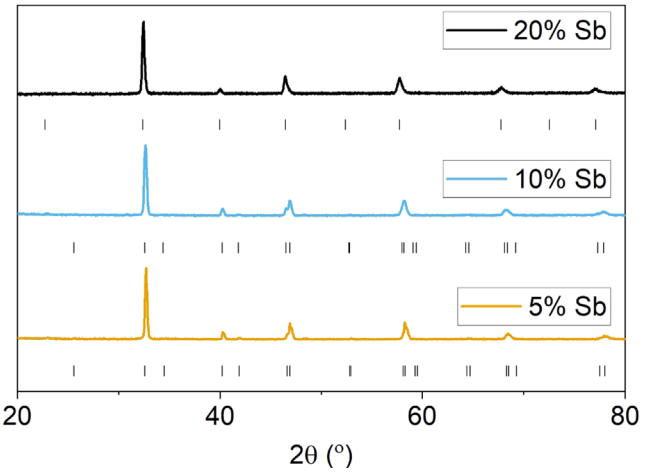

Figure 1. X-ray diffraction patterns for the synthesized $SrCo_{1-x}Sb_xO_{3-\delta}$ powders. Observed reflections were compared to those published by Aguadero et al.[40] and displayed below the relevant pattern.

Samples were heated to 1000 °C at a rate of 10 °C min^{-1} under an argon flow rate of 100 ml min^{-1}. The oxygen levels were converted from ppm by calibrating the oxygen sensor with known flow rates of 2% oxygen:argon. Prior to each experiment, each powder was held at 135 °C for 25 min to stabilize the mass signal and try to remove as much excess water adsorbed on the sample surface. The change in mass was converted to oxygen non-stoichiometry values using Eq. 3. Initial non-stoichiometry values were obtained from previously published X-ray Absorption Near Edge Spectroscopy experiments.[43]

$$\Delta\delta = \frac{\Delta m \cdot M_s}{m_0 \cdot M_O} \quad [3]$$

where $\Delta\delta$ is change in stoichiometry, Δm is change in mass, m_0 is the initial mass, M_s and M_O are the molecular weight of the synthesized sample and atomic mass of oxygen respectively.

Systematic errors were minimized by carrying out an identical run with an empty crucible and the sample masses were sufficiently large to reduce to uncertainties to below 0.001%.

Kinetic analysis through isothermal gas switching.—Isothermal redox cycling experiments were carried out using the same simultaneous thermal analysis instrument. A similar mass of test powder was heated to the target temperature (500 to 800 °C) and gas flow was switched between nitrogen and synthetic air (80% nitrogen, 20% oxygen) every 20 min. The change in mass and DSC signal were recorded using the same software.

Density functional theory and Bader charge analysis.—Spin-polarized density functional theory calculations were performed using the Vienna Ab Initio Simulation Package (VASP) version 5.4.4[44] using the Perdew–Burke–Ernzerhof (PBE) exchange–correlation functional.[45] Projector-augmented wave (PAW) pseudopotentials were used for all species, with a plane wave cut off of 520 eV.[46] An initial undoped $SrCoO_3$ structure was obtained from the Materials Project [47](mp-1273854). The lattice parameters and atomic positions were fully relaxed until the force on any atom fell below 0.01 eV Å with an electronic convergence of 1×10^{-6} eV. To model the effect of correlation of cobalt d-electrons, the DFT + U method[48,49] was used with a U correction of 3.32 eV taken from previous work.[50] Sb substitution was investigated by replacing one Co with a Sb dopant in a 32 f.u. $SrCoO_3$ supercell. The atomic positions and lattice parameters of the Sb doped $SrCoO_3$ supercell

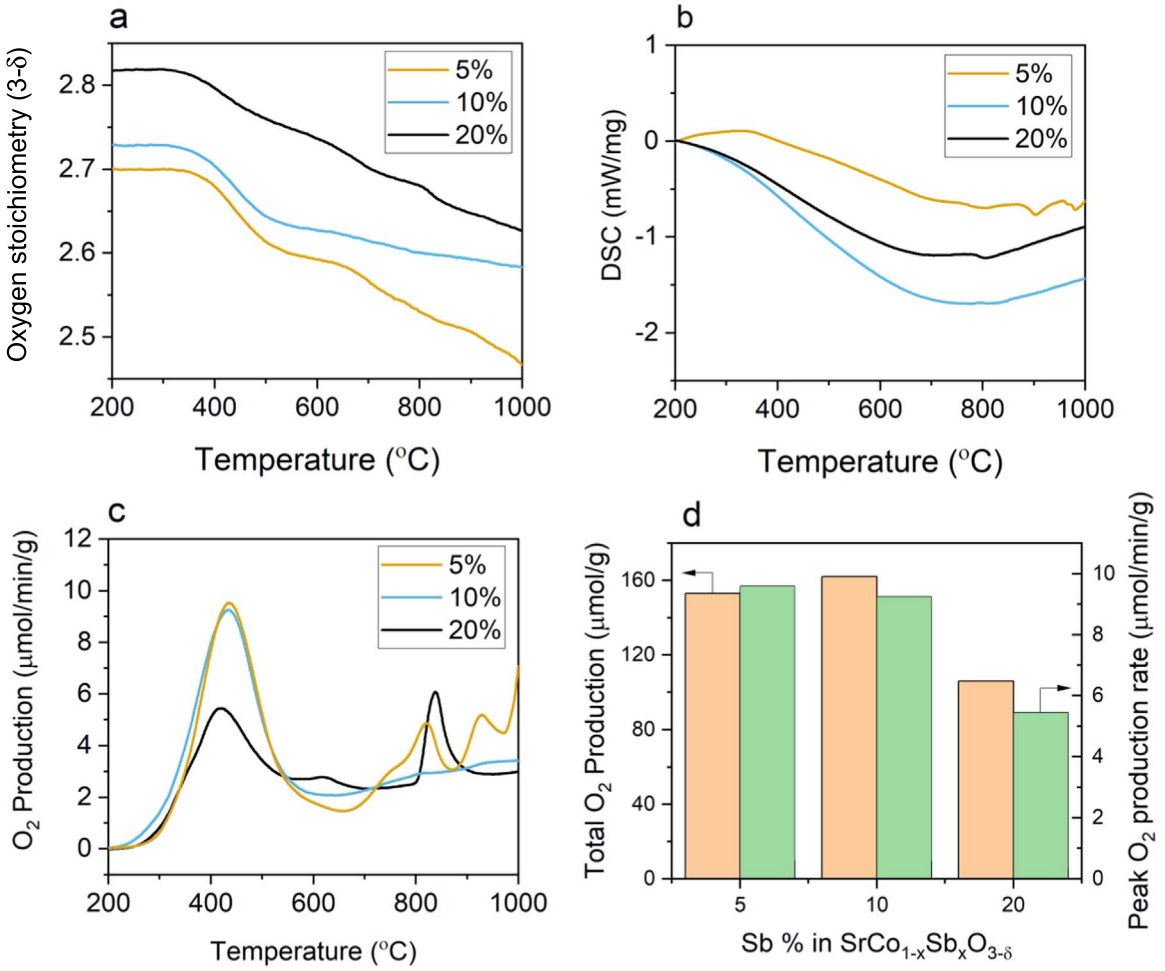

Figure 2. (a) Oxygen stoichiometry, (b) DSC and (c) O_2 production behavior as a function of temperature when heating under an argon flow. (d) Comparison of total O_2 production and peak production as a function of dopant concentration.

Table I. DFT results comparing the undoped and 3.125% doped *P4/mmm* structures.

	$SrCoO_3$	$SrCo_{0.96875}Sb_{0.03125}O_3$
O 2p Band Centre (eV)	−1.22	−1.16
Defect structure formula	$SrCoO_{2.96875}$	$SrCo_{0.96875}Sb_{0.03125}O_{2.96875}$
Oxygen non-stoichiometry	0.03125	0.03125
Sb-O-Co Vacancy Formation (eV)	n/a	1.13
Second Coordination Sphere Co-O-Co Vacancy Formation (eV)	0.59	0.29
Third Coordination Sphere Co-O-Co Vacancy Formation (eV)	n/a	0.51

were subsequently relaxed. The Brillouin zone was sampled using a 2 × 2 × 2 gamma-centred k-point mesh during the geometry optimization of the $SrCo_{1-x}Sb_xO_3$ supercells. Final energies of structures were calculated using single-point calculations with the Blöchl tetrahedron method and a 4 × 4 × 4 gamma-centered k-point mesh.

The density of states and Bader charge densities were calculated using codes developed by the Henkelman group.[51,52] The enthalpy of reduction at 0 K, ΔH_{red}, was calculated using Eq. 4. The oxygen molecule energy was computed through geometric relaxation of the molecule within a 12 × 12 × 12 Å rhombohedral cell. A single oxygen ion was removed from the first coordination sphere of the dopant, and separately from the second coordination sphere to simulate the Sb–O–Co and Co–O–Co environments respectively. The atomic positions were relaxed under fixed cell conditions using the same parameters as the oxygen stoichiometric cells.

$$\Delta H_{red} = E_{ABO_{3-\delta}} + \frac{1}{2}E_{O_2} - E_{ABO_3} \quad [4]$$

where E_{ABO_3}, $E_{ABO_{3-\delta}}$ and E_{O_2} are the relaxed energies of the pristine, vacancy-defected and oxygen gas structures respectively. An anion correction 0.70 eV per O atom was applied to correct for the overbinding of the O_2 molecule, as previously discussed by Wang et al.[50] and implemented within the pymatgen analysis code.[53]

Results and Discussion

Crystallographic and morphological characterization.—The crystal structures of as synthesized powder samples were characterized using X-ray diffraction. Figure 1 shows the XRD patterns confirming the 5% and 10% antimony-substituted samples matched

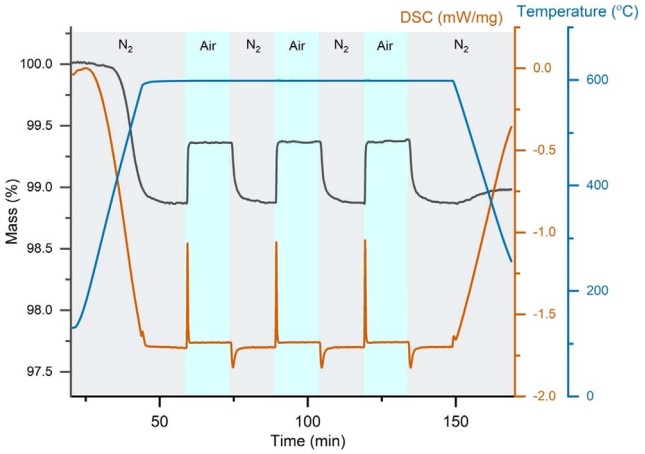

Figure 3. Redox cycling results for $SrCo_{0.90}Sb_{0.10}O_{3-\delta}$ at 600 °C.

with the *P*4/*mmm* tetragonal structure, whereas the 20% dopant concentration stabilized the $Pm\ \bar{3}\ m$ cubic polymorph at room temperature, as expected from previous reports in the literature, none of which had any impurity phases detectable.[40,41] Scanning electron microscopy revealed that for all of the prepared powders the particle size was in the range of 10 to 50 μm (Fig. SI1 (available online at stacks.iop.org/JES/169/044509/mmedia)) and the microstructure was similar to that previously reported.[40]

Thermal behavior under inert gas flow and simulating lattice oxygen reduction.—The powders were heated under a dry argon atmosphere in a simultaneous thermogravimetric analyzer in order to understand their behavior during the reduction step. Figures 2a–2c show the TGA, DSC and oxygen evolution results. The TGA shows that the onset of the mass loss was at a temperature between 300 and 400 °C (Fig. SI2). This mass loss can be attributed to the lattice reduction as it coincides with the large broad endothermic energy uptake in the DSC signal and the increase in oxygen level detected in the exhaust stream. This reduction reaction starts at slightly lower temperatures than those previously observed under compressed air due to the lower oxygen partial pressure.[40]

The DSC signals of all the compounds display small endothermic peaks at temperatures above 800 °C. These features correlate with the onset of further mass loss and oxygen production. Previously, these features have been attributed to the phase transitions between the tetragonal to cubic perovskite polymorphs.[40] As the vacancy concentration increases, the average B-site ionic radius increases with the cation reduction thereby leading to a reduction in the Goldschmidt tolerance factor, favoring the crystal structure transformation to cubic symmetry. The 20% doped sample does not

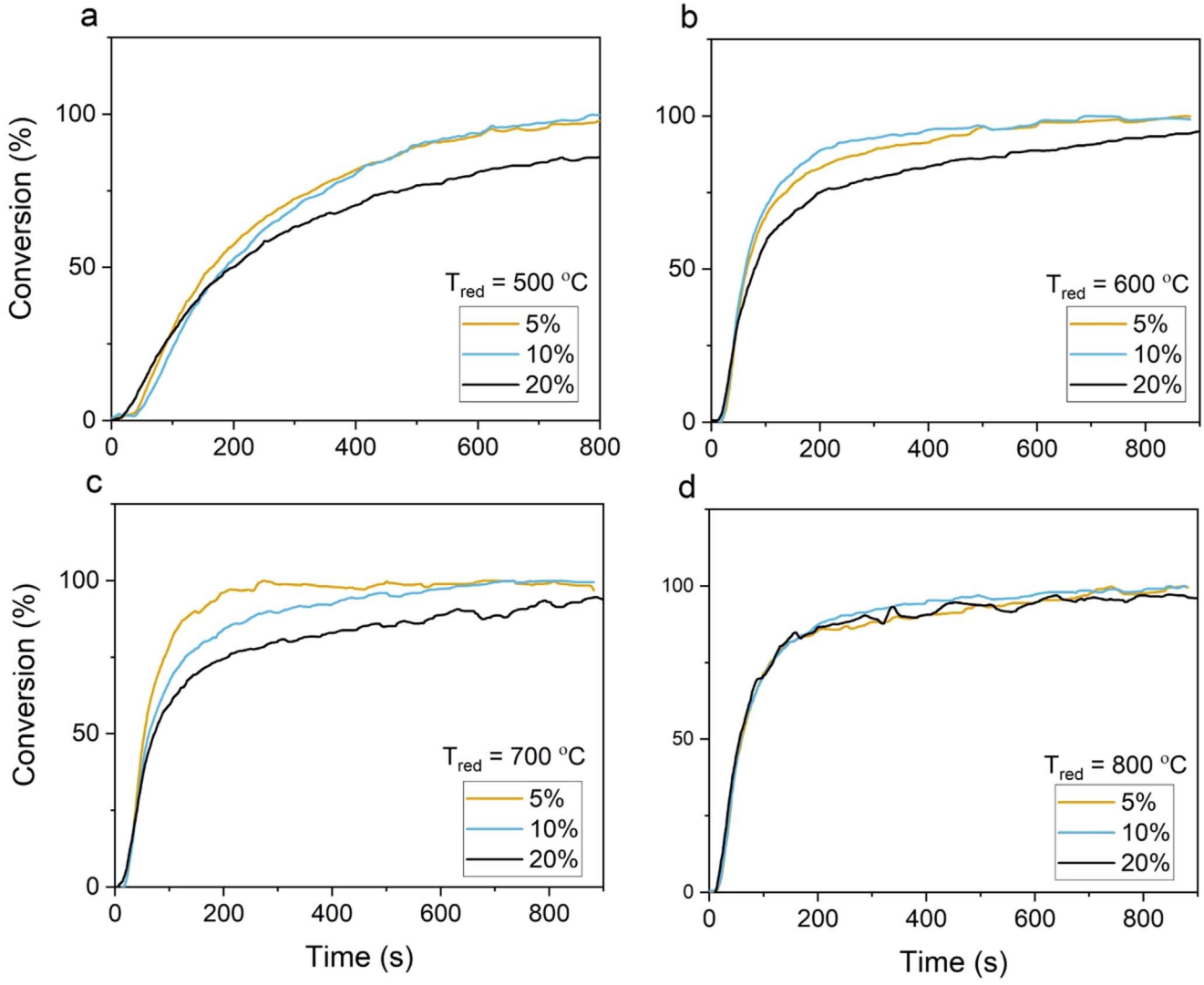

Figure 4. Comparison between the reduction reaction conversion at (a) 500, (b) 600, (c) 700 and (d) 800 °C.

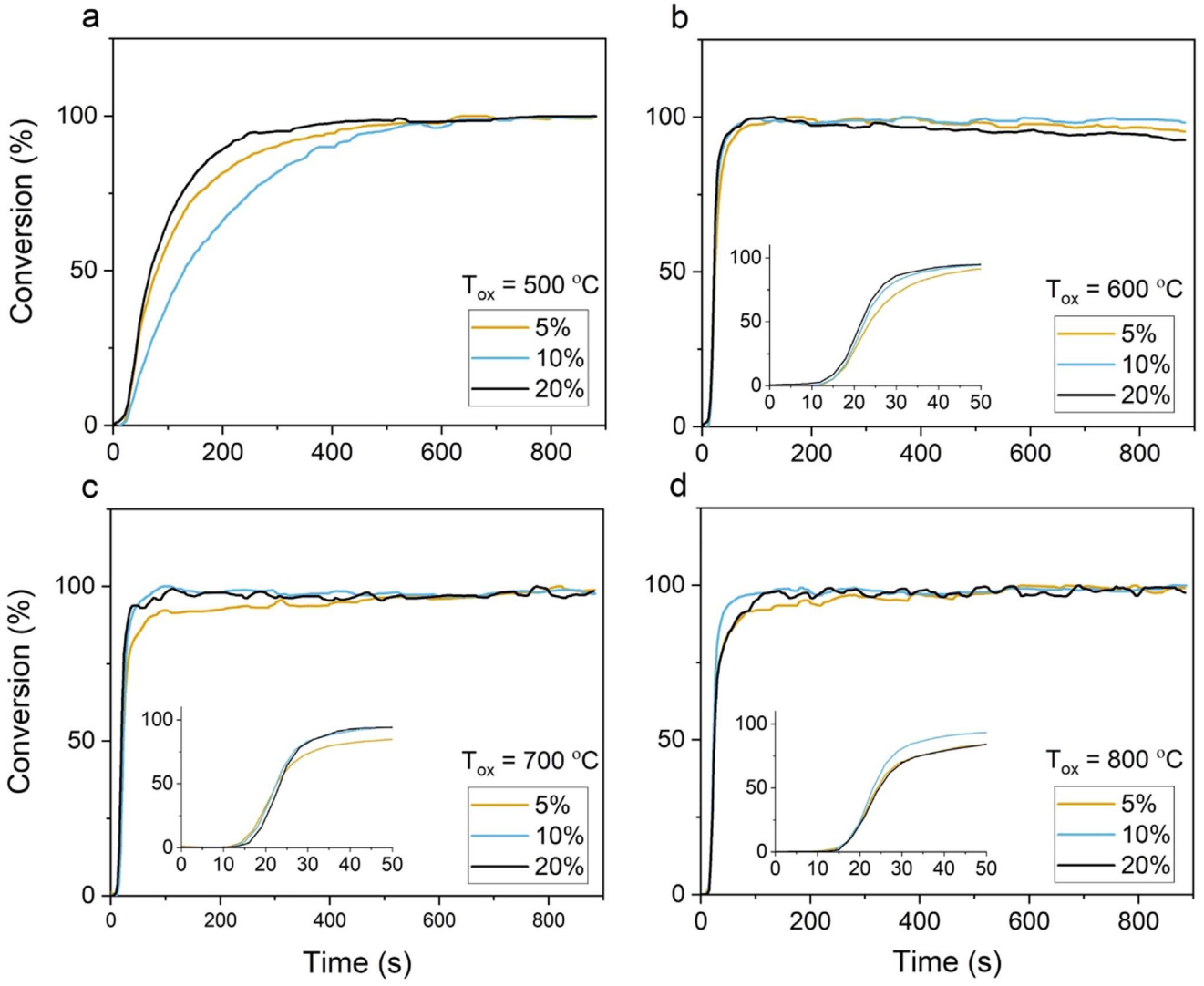

Figure 5. Comparison between the oxidation reaction conversion at (a) 500, (b) 600, (c) 700 and (d) 800 °C.

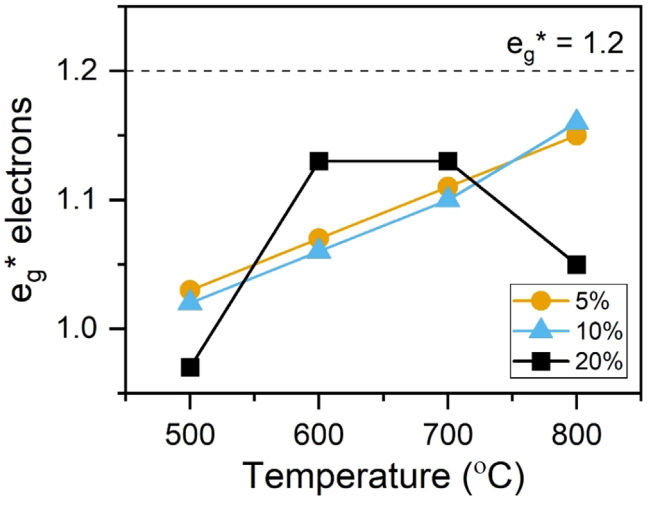

Figure 6. Comparison between number of e_g* electrons as a function of temperature under an argon flow.

demonstrate this arrest in the thermogravimetric signal due to this phase crystallizing in the cubic polymorph. The isothermal redox cycling experiments discussed later in this report had a maximum of 800 °C and therefore are absent from the kinetics study.

Figure 2d compares the total oxygen production and production rate (initial peak) for each of the samples tested up to 800 °C. The 5 and 10% Sb compounds observe similar oxygen production rates to those reported by Ezbiri et al. for $SrCoO_{3-\delta}$ (12.1 μmol min^{-1} g^{-1}).[31] Despite the antimony dopant increasing the average cobalt valency and consequently reducing the inherent oxygen vacancy,[54] the overall oxygen production volume decreases with increasing dopant concentration. This is further understood through density functional theory calculations.

Structures analogous to those experimentally tested were geometrically relaxed to find the lowest energy ground state. Oxygen anions were removed from the structure to create vacancies in the first and second coordination sphere of the antimony dopant. Table I shows the results from the vacancy and density of state calculations. We observe the vacancy formation energy for the anions in the first coordination sphere to be significantly higher, in agreement with the previous investigation by Chen et al. on Sc^{3+} doped strontium cobaltates.[55] Anion vacancy formation becomes more facile in the

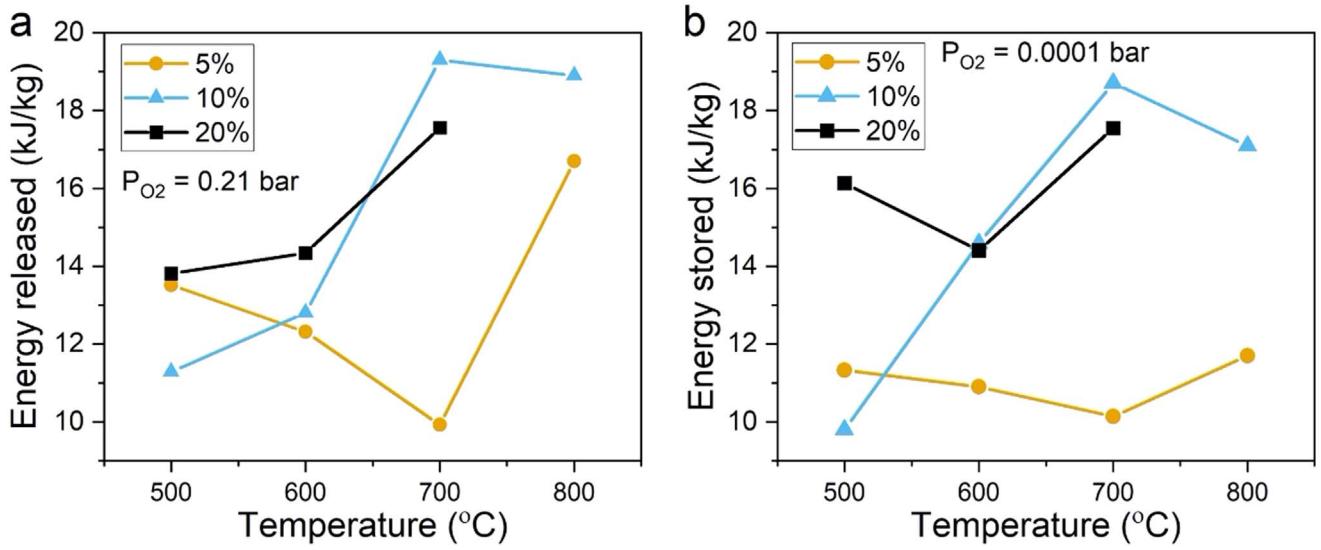

Figure 7. Comparison between thermal energy (a) stored and (b) released in the first cycle as calculated through the integration of the DSC signals.

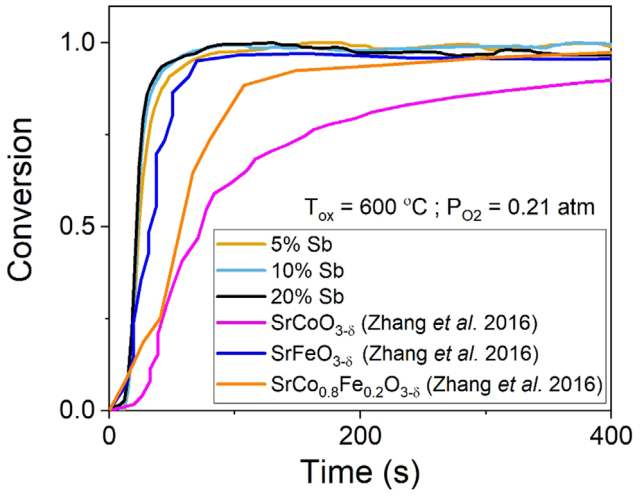

Figure 8. Comparison of oxidation conversion at 600 °C to literature materials reported by Zhang et al.[18]

second coordination sphere with introduction of the Sb dopant. We postulate that the antimony dopant creates an inductive effect on the neighboring cobalt cations: the increased electronegativity of Sb results in a covalent Sb-O bond that in turn induces more ionic O-Co bonds.[54] The increased ionicity is also revealed from the analysis of the density of states (Fig. SI3) which displays the O 2p band center moving closer to the Fermi energy. Previous authors have correlated this oxygen evolution from the lattice and improvements in lattice oxygen migration.[56,57] Furthermore, this can help explain the previous oxygen migration observations in $SrCo_{1-x}Sb_xO_{3-\delta}$ perovskites.[40,55,58] The lower volume of oxygen evolved from the higher Sb content samples (Fig. 2d) can be associated with the increased concentration of strong Sb-O covalent bonds with significantly higher reduction enthalpy. The antimony with nominal oxidation state Sb^{5+} requires greater electron transfer for reduction to the stable Sb^{3+} oxidation state.

Isothermal redox cycling and energy storage.—The isothermal redox kinetics were investigated using both TGA and DSC. The powders were heated to a given temperature between 500 and 800 °C, once the temperature was stabilized, consecutive cycles of reduction and oxidation using nitrogen and compressed air, respectively, were performed. Three cycles were completed for each powder before cooling to room temperature. Figure 3 shows an example of the 10% doped powder's redox cycles at 600 °C. Full cycling data for each sample and temperature can be found in Figs SI4 to SI6.

The TGA shows clear mass increase and decrease when the atmosphere is switched between compressed air and nitrogen, respectively. The DSC signal also shows clear exothermic and endothermic peaks for the oxidation and reduction reactions taking place. The integral of these peaks allows for the determination of energy stored or released during the redox cycle. All of the compounds showed good cyclability over the number of cycles. This suggests that the materials are durable under these operating temperatures and atmospheres.

The kinetics of the materials can be studied by plotting the reduction and oxidation conversion vs time during isothermal cycling (Figs. 4a–4d and 5a–5d respectively). Much faster kinetics were observed for oxidation than for reduction in all dopant concentrations. The conversion rate for the oxidation and reduction reactions increased with temperature, thus suggesting both processes were thermally activated. Furthermore, the reduction reaction appears to become more sluggish with increased dopant concentration. Both reactions can be deconvoluted into a surface reaction and bulk diffusion of oxygen through the lattice. Crucially, as has been previously reported, the increment on Sb content is associated with an increase in the Co oxidation state which is associated with oxidation of the lattice and annihilation of oxygen vacancies leading to slower oxygen diffusion.[40] Furthermore, the reductive coupling charge transfer via Co–O–Co bonds becomes disrupted with increased Sb content thereby reducing the electronic conductivity of the material.[40]

Redox kinetics of metal oxide reactions have been proposed to be related to the filling of the e_g* shell. This is due to the strong overlap between metal e_g* orbitals and anion O 2p orbitals forming σ bonds that facilitate fast charge transfer. The highest activity for the oxygen evolution reaction was previously found to occur in other perovskite materials when the e_g* filling was ∼1.2.[59]

The antimony dopant affects the neighboring cobalt cations by lowering the energy difference between the e_g* and t_{2g} bands to induce an intermediate spin state.[43,60] Using the originally published XANES oxidation states we can estimate the number of e_g* electrons at the point immediately before switching to an oxidizing atmosphere. Figure 6 shows that for all compounds the number of e_g* electrons is closer to the ideal value of 1.2 and that with temperature, the number increases. Further increasing the operation temperature would induce

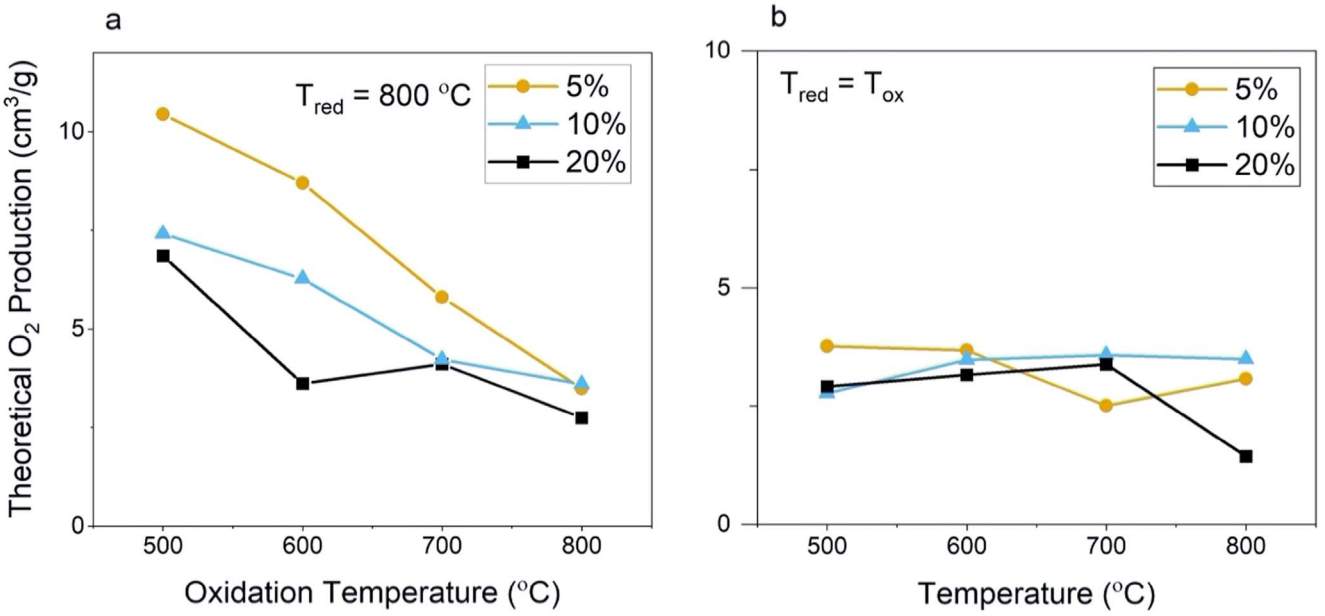

Figure 9. Comparison of theoretical specific capacity under the conditions (a) Temperature Swing (T_{red} = 800 °C) (b) Isothermal (T_{red} = T_{ox}).

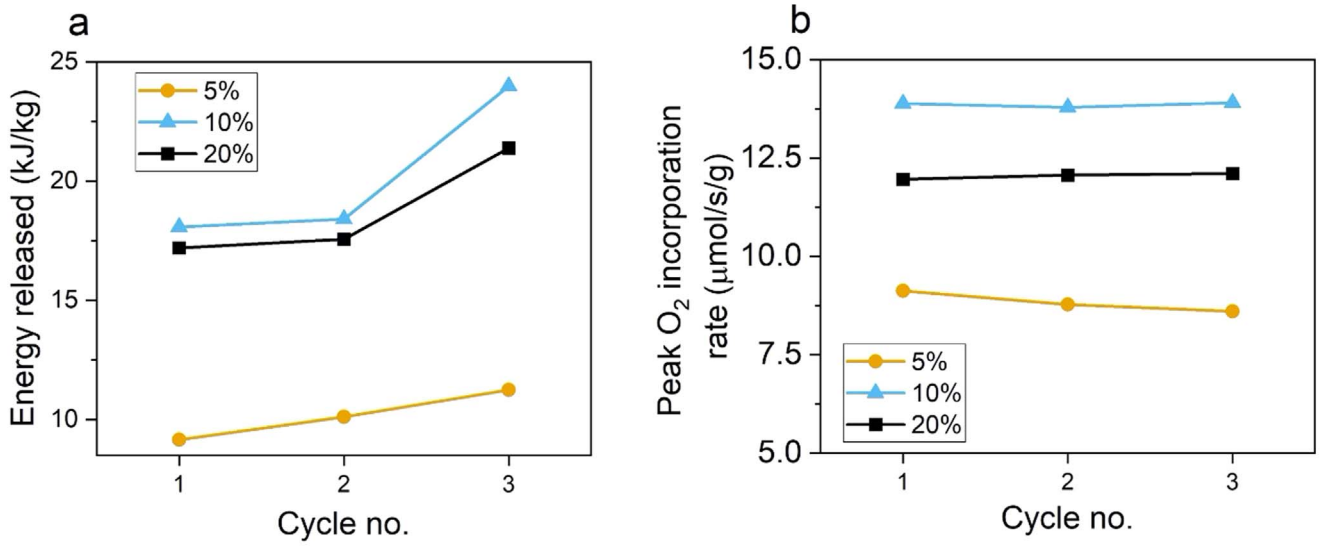

Figure 10. Comparison of (a) energy released and (b) peak O_2 incorporation for each composition over all cycles tested.

the temperature changes to the *Pm* $\bar{3}$ *m* cubic phase and potentially phase degradation if the vacancy concentration becomes too large for the perovskite structure to withstand.

Figures 7a and 7b display the average thermal energy released and stored when isothermally cycling at each of the temperatures. The energy stored by the 10 and 20% compounds increases with temperature whereas the 5% doped compound observes little change. The values were obtained from integrating the exothermic and endothermic peaks for the oxidation and reduction reactions respectively. Due to the isothermal cycling, the energies reported here are purely thermochemical rather than the addition of sensible heat. However, these values are significantly lower than the thermochemical energy stored within other reported perovskites and metal oxides.[12,23] On the other hand, the low temperatures and fast redox kinetics can be used for thermochemical oxygen separation technologies. Comparisons are drawn with similarly synthesized and cycled oxygen separation materials to demonstrate introducing antimony improves the oxidation kinetics of $SrCoO_{3-\delta}$ to comparative levels with the literature benchmark $SrFeO_{3-\delta}$ (Fig. 8).[18]

A theoretical maximum oxygen evolution value can also be calculated through consideration of the maximum and minimum non-stoichiometry values in the isothermal gas switching experiments. Figure 9a compares the theoretical volume of oxygen exchange for each composition when considering a reduction temperature of 800 °C. As expected, this increases when a lower oxidation temperature is used and is significantly higher when compared to an isothermal regime (T_{ox} = T_{red}) as displayed in Fig. 9b. Furthermore, the theoretical production volume decreases with increased dopant concentration which is associated with the increased number stronger covalent Sb-O bonds. The oxygen volumes exchanged under isothermal conditions exceeds the volumes reported for $SrCo_{0.85}Fe_{0.15}O_{3-\delta}$ (1.05 cm^3 g^{-1} at 500 °C and

0.78 cm^3 g^{-1} at 600 °C),[28] although this material observes exceptional performance at 300 °C.

The energy/oxygen stored and released as well as kinetic rates were observed to be reasonably consistent over the number of cycles in this study (Figs. 10a and 10b). The topotactic exchange of oxygen within these compounds has been well-studied when heating and cooling within air.[40,41] The absence of any additional peaks within the DSC signal suggests no adverse reactions that could lead to degradation of the material upon cycling, however post-TGA cycling XRD analysis revealed the presence of secondary phase peaks (Fig. SI6–8). These peaks could be contributions from either $SrCo_6O_{11}$, $Sr_6Co_5O_{15}$ or $Sr_2Sb_2O_7$ phases that have been identified through the DFT calculations as possible decomposition products (Table SI1). These peaks become less apparent with higher doping concentrations thus suggesting better thermal stability of higher doped compounds, as previously reported.[40]

From our discussions above, the level of *B*-site dopant can be tuned to provide the best performance of strontium cobalt oxides for thermochemical energy storage. New dopant investigations would require the improvement of the reduction reaction kinetics in order to balance the rapid oxidation. The reduction reaction can be favored by increasing the electron energy of the O 2p band centre but should also allow facile electron transfer. Furthermore, these dopants would need to be able to lower the crystal field splitting sufficiently to promote the intermediate spin electron configuration and therefore the number of e_g* electrons. Alternative strategies could also be employed to improve the reduction kinetics such as ex-solution,[61] or nanostructuring.[62]

Conclusions

Strontium cobalt oxide has previously been proposed as a promising material for thermochemical oxygen exchange applications. Prior knowledge from the solid oxide fuel cell cathode field has identified B-site doping as a strategy to improve the oxygen exchange kinetics of these materials. Here we investigated the performance of a series of antimony doped compounds as thermochemical oxygen exchange materials due to their fast redox kinetics and high oxygen storage capabilities.

We propose that the antimony dopant has an inductive effect on neighboring cobalt cations thereby changing the electronic structure and promoting lattice oxygen evolution, but ultimately reduction performance is limited by the concentration of strong Sb-O covalent bonds and slow oxygen diffusion within the bulk due to oxygen vacancy annihilation due to the oxidation of the lattice promoted by the incorporation of Sb. However, the inclusion of the dopant lowers the d-orbital energy splitting to allow for increased e_g* orbital filling and consequently faster electron charge transfer kinetics. The low energy released and stored during the redox processes suggested these materials are better placed in thermochemical air separation applications. The addition of antimony was observed to improve the kinetics compared to the literature reports of the $SrCoO_{3-\delta}$ perovskite. The best performance was demonstrated by the $SrCo_{0.9}Sb_{0.1}O_{3-\delta}$ compound in terms of more equivalent reduction and oxidation kinetics although the 5% doped sample demonstrated higher oxygen evolution volumes (3.76 cm^3 g^{-1} at 500 °C). The combination of experimental and computational data herein allowed for further understanding and better design of new metal oxide compounds for thermochemical redox applications

Acknowledgments

The authors would like to acknowledge Mr Richard Sweeney from the Imperial College London Materials department's XRD and Thermal Analysis suite and wish him a happy and well-deserved retirement. Further acknowledgements are to the Harvey Flowers Electron Microscopy suite at Imperial College London, the Imperial College Research Computing Service (10.14469/hpc/2232), and other associated support services used during this work.

Funding

Funding for this work was provided by EPSRC CDT in Fuel Cells and their fuels: EP/L015749/1. SJS, AA and IDS thank the EPSRC for funding through a Platform funding award (EP/R002010/1).

ORCID

Stephen J. Skinner https://orcid.org/0000-0001-5446-2647

References

1. L. A. Weinstein, J. Loomis, B. Bhatia, D. M. Bierman, E. N. Wang, and G. Chen, "Concentrating solar power." *Chem. Rev.*, **115**, 12797 (2015).
2. Q. Peng, X. Yang, J. Ding, X. Wei, and J. Yang, "Design of new molten salt thermal energy storage material for solar thermal power plant." *Appl. Energy*, **112**, 682 (2013).
3. N. Breidenbach, C. Martin, H. Jockenhöfer, and T. Bauer, "Thermal energy storage in molten salts: overview of novel concepts and the DLR test facility TESIS." *Energy Procedia*, **99**, 120 (2016).
4. D. Laing, C. Bahl, T. Bauer, M. Fiss, N. Breidenbach, and M. Hempel, "High-temperature solid-media thermal energy storage for solar thermal power plants." *Proc. IEEE*, **100**, 516 (2012).
5. M. M. Kenisarin, "High-temperature phase change materials for thermal energy storage." *Renew. Sust. Energ. Rev.*, **14**, 955 (2010).
6. A. J. Carrillo, J. Gonzalez-Aguilar, M. Romero, and J. M. Coronado, "Solar energy on demand: a review on high temperature thermochemical heat storage systems and materials." *Chem. Rev.*, **119**, 4777 (2019).
7. D. A. Sheppard et al., "Metal hydrides for concentrating solar thermal power energy storage." *Appl. Physics A*, **122**, 395 (2016).
8. L. André and S. Abanades, "Evaluation and performances comparison of calcium, strontium and barium carbonates during calcination/carbonation reactions for solar thermochemical energy storage." *J. Energy Storage*, **13**, 193 (2017).
9. M. Benitez-Guerrero, J. M. Valverde, P. E. Sanchez-Jimenez, A. Perejon, and L. A. Perez-Maqueda, "Multicycle activity of natural $CaCO_3$ minerals for thermochemical energy storage in Concentrated Solar Power plants." *Sol. Energy*, **153**, 188 (2017).
10. Y. A. Criado, M. Alonso, and J. C. Abanades, "Kinetics of the CaO/$Ca(OH)_2$ Hydration/Dehydration Reaction for Thermochemical Energy Storage Applications." *Ind. Eng. Chem. Res.*, **53**, 12594 (2014).
11. G. Gravogl et al., "Cycle stability and hydration behavior of magnesium oxide and its dependence on the precursor-related particle morphology." *Nanomaterials*, **8**, 795 (2018).
12. C. Agrafiotis, M. Roeb, M. Schmücker, and C. Sattler, "Exploitation of thermochemical cycles based on solid oxide redox systems for thermochemical storage of solar heat. Part 1: testing of cobalt oxide-based powders." *Sol. Energy*, **102**, 189 (2014).
13. M. Neises, S. Tescari, L. de Oliveira, M. Roeb, C. Sattler, and B. Wong, "Solar-heated rotary kiln for thermochemical energy storage." *Sol. Energy*, **86**, 3040 (2012).
14. A. J. Carrillo, J. L. M. Rupp, and J. M. Coronado, "Redox oxides for thermochemical energy storage." *Energy Storage and Conversion Materials*, ed. S. J. Skinner (Inorganic Materials Series, RSC, Cambridge, UK) (2019).
15. K. N. Hutchings, M. Wilson, P. A. Larsen, and R. A. Cutler, "Kinetic and thermodynamic considerations for oxygen absorption/desorption using cobalt oxide." *Solid State Ionics*, **177**, 45 (2006).
16. T. Block and M. Schmücker, "Metal oxides for thermochemical energy storage: a comparison of several metal oxide systems." *Sol. Energy*, **126**, 195 (2016).
17. A. J. Carrillo, D. P. Serrano, P. Pizarro, and J. M. Coronado, "Manganese oxide-based thermochemical energy storage: modulating temperatures of redox cycles by Fe–Cu co-doping." *J. Energy Storage*, **5**, 169 (2016).
18. Z. Zhang, L. Andre, and S. Abanades, "Experimental assessment of oxygen exchange capacity and thermochemical redox cycle behavior of Ba and Sr series perovskites for solar energy storage." *Sol. Energy*, **134**, 494 (2016).
19. L. Imponenti, K. J. Albrecht, R. Kharait, M. D. Sanders, and G. S. Jackson, "Redox cycles with doped calcium manganites for thermochemical energy storage to 1000 ° C." *Appl. Energy*, **230**, 1 (2018).
20. R. Le Toquin, W. Paulus, A. Cousson, C. Prestipino, and C. Lamberti, "Time-resolved in situ studies of oxygen intercalation into $SrCoO_{2.5}$ performed by neutron diffraction and X-ray absorption spectroscopy." *J. Am. Chem. Soc.*, **128**, 13161 (2006).
21. S. M. Babiniec, E. N. Coker, J. E. Miller, and A. Ambrosini, "Investigation of $La_xSr_{1-x}Co_yM_{1-y}O_{3-\delta}$ (M = Mn, Fe) perovskite materials as thermochemical energy storage media." *Sol. Energy*, **118**, 451 (2015).
22. S. M. Babiniec, E. N. Coker, J. E. Miller, and A. Ambrosini, "Doped calcium manganites for advanced high-temperature thermochemical energy storage." *Int. J. Energy Res.*, **40**, 280 (2016).
23. L. Imponenti, K. J. Albrecht, J. W. Wands, M. D. Sanders, and G. S. Jackson, "Thermochemical energy storage in strontium-doped calcium manganites for concentrating solar power applications." *Sol. Energy*, **151**, 1 (2017).
24. Q. Imtiaz, D. Hosseini, and C. R. Müller, "Review of oxygen carriers for chemical looping with oxygen uncoupling (CLOU): thermodynamics, material development, and synthesis." *Energy Technol.*, **1**, 633 (2013).

25. E. Krzystowczyk, X. Wang, J. Dou, V. Haribal, and F. Li, "Substituted $SrFeO_3$ as robust oxygen sorbents for thermochemical air separation: correlating redox performance with compositional and structural properties." *Phys. Chem. Chem. Phys.*, **22**, 8924 (2020).
26. J. Dou, E. Krzystowczyk, X. Wang, A. R. Richard, T. Robbins, and F. Li, "$Sr_{1-x}Ca_xFe_{1-x}Co_xO_{3-\delta}$ as facile and tunable oxygen sorbents for chemical looping air separation." *J. Phys.: Energy*, **2**, 025007 (2020).
27. B. Bulfin, J. Lapp, S. Richter, D. Guban, J. Vieten, S. Brendelberger, M. Roeb, and C. Sattler, "Air separation and selective oxygen pumping via temperature and pressure swing oxygen adsorption using a redox cycle of $SrFeO_3$ perovskite." *Chem. Eng. Sci.*, **203**, 68 (2019).
28. H. Ikeda, A. Tsuchida, J. Morita, and N. Miura, "$SrCo_xFe_{1-x}O_{3-\delta}$ oxygen sorbent usable for high-temperature pressure-swing adsorption process operating at approximately 300 °C." *Ind. Eng. Chem. Res.*, **55**, 6501 (2016).
29. J. Dou, E. Krzystowczyk, X. Wang, T. Robbins, L. Ma, X. Liu, and F. Li, "A- and B-site codoped $SrFeO_3$ oxygen sorbents for enhanced chemical looping air separation." *ChemSusChem*, **13**, 385 (2020).
30. G. Luongo, F. Donat, and C. R. Müller, "Structural and thermodynamic study of Ca A- or Co B-site substituted $SrFeO_{3-\delta}$ perovskites for low temperature chemical looping applications." *Phys. Chem. Chem. Phys.*, **22**, 9272 (2020).
31. M. Ezbiri, K. M. Allen, M. E. Gàlvez, R. Michalsky, and A. Steinfeld, "Design principles of perovskites for thermochemical oxygen separation." *ChemSusChem*, **8**, 1966 (2015).
32. V. Cascos, R. Martínez-Coronado, and J. A. Alonso, "New Nb-doped $SrCo_{1-x}Nb_xO_{3-\delta}$ perovskites performing as cathodes in solid-oxide fuel cells." *Int. J. Hydrog. Energy*, **39**, 14349 (2014).
33. A. Aguadero, D. Pérez-Coll, J. A. Alonso, S. J. Skinner, and J. Kilner, "A new family of Mo-doped $SrCoO_{3-\delta}$ perovskites for application in reversible solid state electrochemical cells." *Chem. Mater.*, **24**, 2655 (2012).
34. V. Cascos, L. Troncoso, M. T. Fernández-Diaz, and J. A. Alonso, "$SrCo_{1-x}Ru_xO_{3-\delta}$ ($x = 0.05$, 0.1, and 0.15) perovskites as outperforming cathode material in intermediate-temperature solid oxide fuel cells." *ACS Appl. Energy Mater.*, **1**, 4505 (2018).
35. R. E. Usiskin, T. C. Davenport, R. Y. Wang, W. Guan, and S. M. Haile, "Bulk properties of the oxygen reduction catalyst $SrCo_{0.9}Nb_{0.1}O_{3-\delta}$." *Chem. Mater.*, **28**, 2599 (2016).
36. Y. Pan et al., "Direct evidence of boosted oxygen evolution over perovskite by enhanced lattice oxygen participation." *Nat. Commun.*, **11**, 2002 (2020).
37. W. T. A. Harrison, S. L. Hegwood, and A. J. Jacobson, "A powder neutron diffraction determination of the structure of $Sr_6Co_5O_{15}$, formerly described as the low-temperature hexagonal form of $SrCoO_{3-x}$." *J. Chem. Soc., Chem. Commun.*, 1953 (1995).
38. K. Iwasaki, H. Yamane, T. Murase, M. Yoshino, T. Ito, T. Nagasaki, Y. Arita, and T. Matsui, "Crystal structure of an oxygen deficient strontium cobaltate, $Sr_6Co_5O_{14.3}$." *J. Ceram. Soc. Japan*, **117**, 89 (2009).
39. A. Aguadero, C. de la Calle, J. A. Alonso, M. J. Escudero, M. T. Fernandez-Diaz, and L. Daza, "Structural and electrical characterization of the novel $SrCo_{0.9}Sb_{0.1}O_{3-\delta}$ perovskite: evaluation as a solid oxide fuel cell cathode material." *Chem. Mater.*, **19**, 6437 (2007).
40. A. Aguadero, D. Perez-Coll, C. de la Calle, J. A. Alonso, M. J. Escudero, and L. Daza, "$SrCo_{1-x}Sb_xO_{3-\delta}$ perovskite oxides as cathode materials in solid oxide fuel cells." *J. Power Sources*, **192**, 132 (2009).
41. A. Aguadero, J. A. Alonso, D. Perez-Coll, C. de la Calle, M. T. Fernandez-Diaz, and J. B. Goddenough, "$SrCo_{0.95}Sb_{0.05}O_{3-\delta}$ as cathode material for high power density solid oxide fuel cells." *Chem. Mater.*, **22**, 789 (2010).
42. A. Cavallaro, G. E. Wilson, G. Kerherve, E. Cali, C. A. M. van den Bosch, P. Boldrin, D. Payne, S. J. Skinner, and A. Aguadero, "Analysis of H_2O-induced surface degradation in $SrCoO_3$ derivatives and its impact on redox kinetics." *J. Mater. Chem. A*, **9**, 24528 (2021).
43. A. Aguadero, M. Retuerto, F. Jiménez-Villacorta, M. T. Fernandez-Diaz, and J. A. Alonso, "Evolution of cobalt spin states and magnetic coupling along the $SrCo_{1-x}Sb_xO_{3-\delta}$ system: Correlation with the crystal structure." *Phys. Chem. Chem. Phys.*, **13**, 12835 (2011).
44. G. Kresse and J. Furthmüller, "Efficient iterative schemes for ab initio total-energy calculations using a plane-wave basis set." *Phys. Rev. B—Condens. Matter Mater. Phys.*, **54**, 11169 (1996).
45. J. P. Perdew, K. Burke, and M. Ernzerhof, "Generalized gradient approximation made simple." *Phys. Rev. Lett.*, **77**, 3865 (1996).
46. P. E. Blöchl, "Projector augmented-wave method." *Phys. Rev. B*, **50**, 17953 (1994).
47. A. Jain et al., "Commentary: the materials project: a materials genome approach to accelerating materials innovation." *APL Mater.*, **1**, 11002 (2013).
48. V. I. Anisimov, J. Zaanen, and O. K. Andersen, "Band theory and mott insulators: hubbard U instead of stoner I." *Phys. Rev. B*, **44**, 943 (1991).
49. S. Dudarev and G. Botton, "Electron-energy-loss spectra and the structural stability of nickel oxide: an LSDA + U study." *Phys. Rev. B—Condens. Matter Mater. Phys.*, **57**, 1505 (1998).
50. L. Wang, T. Maxisch, and G. Ceder, "Oxidation energies of transition metal oxides within the GGA + U framework." *Phys. Rev. B*, **73**, 195107 (2006).
51. G. Henkelman, A. Arnaldsson, and H. Jónsson, "A fast and robust algorithm for Bader decomposition of charge density." *Comput. Mater. Sci.*, **36**, 354 (2006).
52. W. Tang, E. Sanville, and G. Henkelman, "A grid-based Bader analysis algorithm without lattice bias." *J. Phys. Condens. Matter*, **21**, 84204 (2009).
53. S. P. Ong, W. D. Richards, A. jain, G. Hautier, M. Kocher, S. Cholia, D. Gunter, V. L. Chevrier, K. A. Persson, and G. Ceder, "Python materials genomics (pymatgen): a robust, open-source python library for materials analysis." *Comput. Mater. Sci.*, **68**, 314 (2013).
54. A. Aguadero, M. Retuerto, F. Jiménez-Villacorta, M. T. Fernandez-Diaz, and J. A. Alonso, "Evolution of cobalt spin states and magnetic coupling along the $SrCo_{1-x}Sb_xO_{3-\delta}$ system: correlation with the crystal structure." *Phys. Chem. Chem. Phys.*, **13**, 12835 (2011).
55. D. Chen, C. Chen, Z. Zhang, Z. M. Baiyee, F. Ciucci, and Z. Shao, "Compositional engineering of perovskite oxides for highly efficient oxygen reduction reactions." *ACS Appl. Mater. Interfaces*, **7**, 8562 (2015).
56. T. T. Mayeshiba and D. D. Morgan, "Factors controlling oxygen migration barriers in perovskites." *Solid State Ionics*, **296**, 71 (2016).
57. W. Xie, Y.-L. Lee, Y. Shao-Horn, and D. Morgan, "Oxygen point defect chemistry in ruddlesden–popper oxides $(La_{1-x}Sr_x)_2MO_{4\pm\delta}$ (M = Co, Ni, Cu)." *J. Phys. Chem. Lett.*, **7**, 1939 (2016).
58. A. Grimaud, O. Diaz-Morales, B. Han, W. T. Hong, Y.-L. Lee, L. Giordano, K. A. Stoerzinger, M. T. M. Koper, and Y. Shao-Horn, "Activating lattice oxygen redox reactions in metal oxides to catalyse oxygen evolution." *Nat. Chem.*, **9**, 457 (2017).
59. J. Suntivich, K. J. May, H. A. Gasteiger, J. B. Goodenough, and Y. Shao-Horn, "A perovskite oxide optimized for oxygen evolution catalysis from molecular orbital principles." *Science*, **334**, 1383 (2011).
60. V. Primo-Martín and M. Jansen, "Synthesis, structure, and physical properties of cobalt perovskites: $Sr_3CoSb_2O_9$ and $Sr_2CoSbO_{6-\delta}$." *J. Solid State Chem.*, **157**, 76 (2001).
61. Y. Zhu, W. Zhou, R. Ran, Y. Chen, Z. Shao, and M. Liu, "Promotion of oxygen reduction by exsolved silver nanoparticles on a perovskite scaffold for low-temperature solid oxide fuel cells." *Nano Lett.*, **16**, 512 (2016).
62. A. R. Puigdollers, P. Schlexer, S. Tosoni, and G. Pacchioni, "Increasing oxide reducibility: the role of metal/oxide interfaces in the formation of oxygen vacancies." *ACS Catal.*, **7**, 6493 (2017).